

# Magnetic Imaging of Biomaterials with a Quantum Diamond Microscope

A Major Qualifying Project submitted to the faculty of WORCESTER  
POLYTECHNIC INSTITUTE in partial fulfillment of the requirements for  
the degree of Bachelor of Science in Applied Physics

**Camille McDonnell**

Advised by Raisa Trubko



# WPI

Worcester Polytechnic Institute

Worcester, MA, USA

May 3, 2023

*This report represents the work of one or more WPI undergraduate students submitted to the faculty as evidence of completion of a degree requirement. WPI routinely publishes these reports on its website without editorial or peer review.*

# Contents

<b>List of Figures</b>	<b>iii</b>
<b>List of Tables</b>	<b>v</b>
<b>1 Introduction</b>	<b>2</b>
1.1 Nitrogen-Vacancy Centers in Diamond . . . . .	3
1.2 The Quantum Diamond Microscope . . . . .	7
1.3 QDM Applications to Biology . . . . .	10
1.4 Silk Fibroin Films . . . . .	11
1.5 Goals, Motivations, and Objectives . . . . .	13
<b>2 QDM Measurement Protocol and Background Signal Characterization</b>	<b>15</b>
2.1 QDM Measurement Protocol . . . . .	15
2.2 QDM Background Noise . . . . .	17
2.3 QDM Inhomogeneity . . . . .	19
<b>3 Measuring Silk Fibroin Films</b>	<b>25</b>
3.1 Sample Preparation and Imaging Procedure . . . . .	25
3.2 Measurements of the SF Film Magnetic Signal . . . . .	28
<b>4 Conclusions and Future Work</b>	<b>31</b>



# List of Figures

1.1	NV Diamond . . . . .	3
1.2	NV Diamond Energy Level Transitions . . . . .	4
1.3	ODMR Spectra . . . . .	5
1.4	Zeeman Interaction . . . . .	5
1.5	QDM Image . . . . .	7
1.6	Continuous Wave ODMR Spectra . . . . .	8
1.7	NV Center Orientation . . . . .	9
1.8	Magnetic Field Map . . . . .	9
1.9	QDM Single Cell Imaging . . . . .	10
1.10	QDM Imaging of Tumor Tissue . . . . .	11
1.11	SF Films . . . . .	13
2.1	Etch pits on NV Diamond. . . . .	16
2.2	Example ODMR Spectrum . . . . .	17
2.3	Corrected Magnetic Field Maps to measure QDM background signal . . . . .	18
2.4	Standard Deviation of QDM Background Signal . . . . .	19
2.5	Subsection Areas . . . . .	20
2.6	2hr Subsection Magnetic Field Maps . . . . .	21
2.7	12hr Subsection Magnetic Field Maps . . . . .	22
2.8	24hr Subsection Magnetic Field Maps . . . . .	23

3.1	Burned and Nonburned SF Films . . . . .	26
3.2	SF Film on NV Diamond . . . . .	26
3.3	Subsection Data Analysis . . . . .	28
3.4	Magnetic Signal of SF Films . . . . .	29
3.5	Paramagnetic and Ferromagnetic Components of SF Films . . . . .	30

# List of Tables

3.1	Optimal laser power (W) and run time (hr) for each SF film sample. . . . .	27
-----	--	----

# Abstract

The Quantum Diamond Microscope (QDM) uses ensembles of Nitrogen-Vacancy (NV) centers in diamond to perform high resolution, wide field of view magnetic imaging. An important application of the QDM is magnetic imaging of biological samples to further medical sciences. A sample of particular interest is Silk Fibroin (SF) films doped in magnetic nanoparticles. These samples are a potential therapy for spinal cord regeneration, which is currently not curable. In this work, SF films doped in various concentrations of ferric chloride hexahydrate were imaged and characterized in the QDM for the first time. We showed that higher ferric chloride hexahydrate concentrations result in higher magnetic signal that largely contains paramagnetic properties.

# Acknowledgements

First off, I would like to give a special thanks to my advisor Dr. Raisa Trubko for her generous support and mentorship throughout this project. I am ever grateful for her assistance and guidance throughout my career at WPI to help further my education and passion for quantum science.

Next, I would like to thank Dr. Jeannine Coburn and Ph.D. student Melissa Wojnowski in WPI's Biomedical Engineering Department for providing the Silk Fibroin film samples that were studied.

Finally, I would like to thank Ph.D. students Jacob Feinstein and Aidan Zlotak in WPI's Quantum Sensing Lab for their assistance with this project.

# Chapter 1

## Introduction

Quantum sensing uses quantum technologies, properties, and phenomena to conduct a physical measurement. For an instrument to be considered a quantum sensor it must fall into one of three categories. The first is that the instrument uses a quantum object to measure a physical quantity. The second is that the instrument uses quantum coherence to measure a physical quantity. The third is that the instrument uses quantum entanglement to improve precision and/or sensitivity to beyond the classical limit [3]. When a quantum system falls into one of those categories, making it a quantum sensor, it also performs specific functions. The first function is that the quantum system must have discrete and resolvable energy levels. Secondly, the quantum system must have the capability to be initialized into a known readout state. Finally, the quantum system must interact with a physical quantity such as an electric or magnetic field [3].

The Quantum Diamond Microscope (QDM) is a quantum sensor that uses a Nitrogen-Vacancy (NV) centers in diamond for magnetic imaging. The QDM generates 2D, high resolution, and wide field of view magnetic field maps under a wide range of conditions, most notably in ambient conditions. The capabilities of the QDM make it important for vast applications in fields such as geoscience, biology, and electronics. The QDM has never been used for magnetic imaging of Silk Fibroin (SF) films, which are biomaterials that have promising applications in regeneration therapies [8]. This study was done to experimentally demonstrate how the QDM could be used for magnetic characterization of SF films.

## 1.1 Nitrogen-Vacancy Centers in Diamond

Nitrogen-Vacancy centers are defects in the lattice structure of a diamond where a Nitrogen atom has replaced a Carbon atom adjacent to a vacancy (Fig. 1.1). NV centers have a negative charge ( $NV^-$ ) with six electrons: two from Nitrogen, three from Carbon, and one from the lattice vacancy [7]. Nitrogen-Vacancy centers can exist with an overall neutral ( $NV^0$ ), or positive ( $NV^+$ ) charge states; however, these states are not magneto-optically active, thus sensing is done using the  $NV^-$  charge state [13]. NV centers have built in quantization axes along the NV z-axis [10].

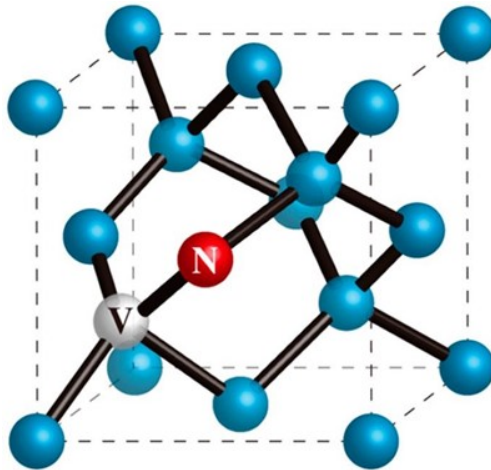


Figure 1.1: NV diamond crystalline lattice. A Nitrogen atom (red) has been substituted for a Carbon atom (blue), generating a vacancy (grey) [7].

The NV centers electrons have  $sp^3$  hybridization, resulting in four atomic molecular orbitals that exist in an integer ( $S=1$ ) spin system. The four molecular orbitals produce the ground and excited state configurations for the NV centers. The ground state of the NV center is the orbital singlet, spin triplet state labeled  $A_2^3$ . The excited state is the orbital doublet, spin triplet state labeled  $E^3$ . The two intermediate states are the orbital singlet, spin singlet states labeled  $E_1^1$  and  $A_1^1$  (Fig. 1.2) [10]. The ground and excited triplet states have three fine levels which are the spin sublevels  $m_s = 0, m_s = +1, m_s = -1$ . The axial symmetry of the NV center cause the  $m_s = \pm 1$  states to be degenerate, and the  $m_s = 0$  state to be lower in energy [13]. The splitting between these spin sublevels is described by the zero-field splitting (ZFS) of 2.87 GHz. Additionally, these fine levels have a zero-phonon line (ZPL) at 637 nm and three of their own hyperfine levels of 0, +1, and -1 [10]. The ZFS and ZPL properties are important for the energy transition between the states.

A key property of NV centers is their radiative and nonradiative energy transitions. To

initiate the radiative or nonradiative energy transitions between the ground and excited state, photons with wavelengths in the range of 460-600 nm are needed [6]. Typically, a 532 nm green laser is used to initiate the energy transition. The transition between the  $A_2^3$  and  $E^3$  state is the radiative process that results in red fluorescence (637 nm) from the NV color-center, matching the ZPL [1]. The transition from  $E^3$  to the intermediate states  $E_1^1$  and  $A_1^1$ , then back to the  $A_2^3$  is the nonradiative process. The nonradiative energy transition is due to the electron-phonon-mediated intercrossing system (ISC) mechanism and is characterized by the ISC rate of transmission [10]. Another important distinction between the different transition processes is that the radiative process conserves spin, while the nonradiative process does not [10].

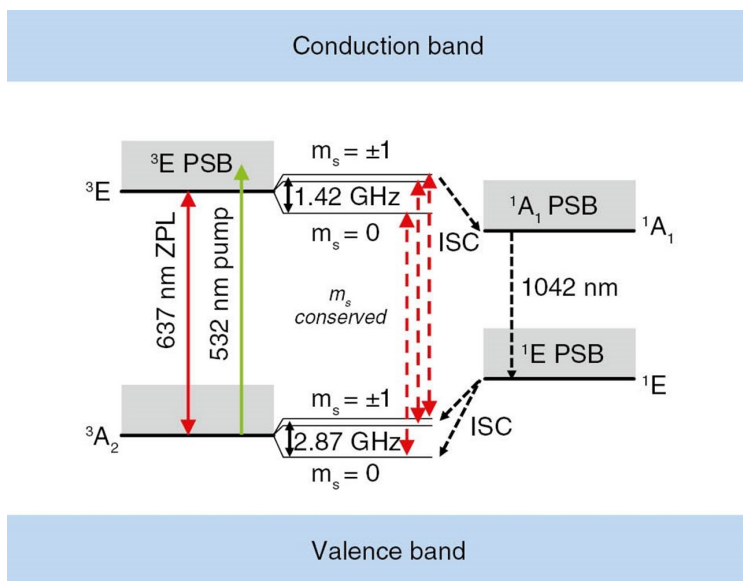


Figure 1.2: NV diamond energy level transitions.  $A_2^3$  is the ground state  $E^3$  is the excited state, and  $E_1^1$  and  $A_1^1$  are the intermediate states [10].

The NV diamond is a unique color center because its fluorescence intensity is coupled to the spin state, thus the fluorescence indicates the spin state of the NV center ( $m_s = 0$  or  $m_s = \pm 1$ ) [13]. This coupling allows for the ability to measure the spin probability distribution of the NV center. The fluorescence intensity can be controlled using a microwave (MW) field where the resonant MW frequency creates ground state electron spin flip transitions from  $m_s = 0$  to  $m_s = \pm 1$ . The fluorescence intensity can be measured using Optically Detected Magnetic Resonance (ODMR) spectroscopy which measures fluorescence intensity as a function of MW frequency. When the NV center is in the  $m_s = \pm 1$  state it emits less fluorescence intensity than in the  $m_s = 0$  state [13]. The ODMR spectra has a Lorentzian line shape, and an example can be seen in Figure 1.3.

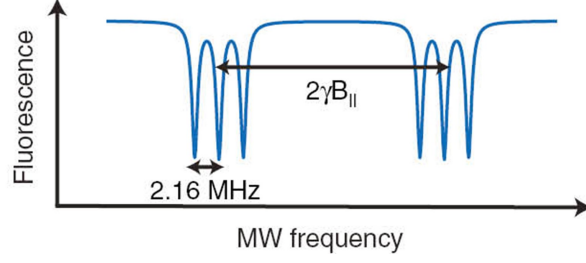


Figure 1.3: Example ODMR Spectra which shows fluorescence intensity as a function of MW frequency [10].

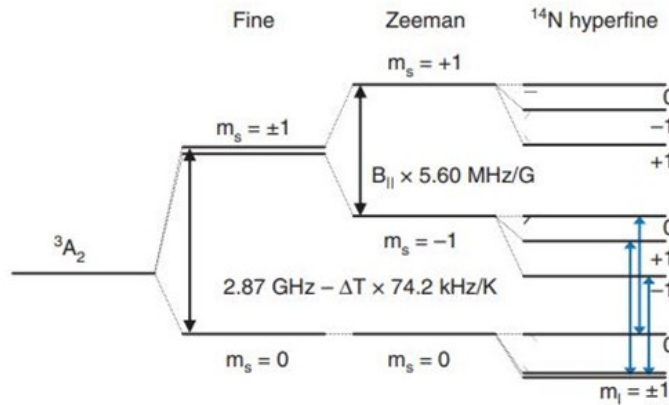


Figure 1.4: NV center ground state energy level diagram with the Zeeman interaction [10].

The purpose of ODMR spectroscopy is to measure magnetic field signals by detecting the NV centers spin dependent fluorescence intensity [13]. The NV centers electron spin is magnetically dependent. Because of this, an external magnetic field causes the Zeeman shift in the NV centers ground state. The Zeeman shift lifts the degeneracy between the  $m_s = \pm 1$  spin sublevels (Fig. 1.4). Lifting the degeneracy means energy transition can be measured between the  $m_s = 0$  state to the  $m_s = +1$  and  $m_s = -1$  states. This measurement creates two resonance dips for the spin sublevel transitions in the ODMR spectra as seen in Figure 1.3 [10]. The three dips in each resonance each corresponds to the energy transition from the  $m_s = 0$  hyperfine states to the  $m_s = +1$  and  $m_s = -1$  hyperfine states (Fig. 1.4). The frequency separation between the resonance dips is characterized by  $2\gamma B_{II}$ , where  $\gamma$  is the electron gyromagnetic ratio  $2\pi * 28 \frac{GHz}{T}$  [13]. This separation allows for measurement of the magnetic field along the NV axis ( $B_{II}$ ).

The ground state NV center Hamiltonian (Eq. 1.1) gives further insight into the properties and characteristics of the NV diamond. The first term is due to the interactions

between the NV center and the magnetic field. The second term is due to electric interactions. The third term is due to crystal strain interaction. The fourth term is due to external temperature variations. The applied, static (bias) magnetic field vector is represented by  $B_0=B_{0x}, B_{0y}, B_{0z}$ . The samples magnetic field vector is represented by  $B_s=B_{sx}, B_{sy}, B_{sz}$ . The electron nuclear spin operator is represented by  $\hat{S}=\hat{S}_x, \hat{S}_y, \hat{S}_z$ . The coupling constants related to the NV electric dipole moment are represented by  $d_{II}$  and  $d_{\perp}$ . The total electric field is the combination of the sample electric field ( $E_s$ ) and the internal local electric fields ( $E_{loc}$ ) in the NV diamond and is represented by  $E_{tot}=E_{tot,x}, E_{tot,y}, E_{tot,z}$ . The stress-dependent amplitudes are represented by  $M_x, M_y, M_z$ . Finally, D(T) is the fine-structure term labeled the zero-field splitting (ZFS) [10].

$$\begin{aligned}
\frac{\hat{H}_{gs}}{h} = & \frac{g_e \mu_b}{h} [(B_{0x} + B_{sx})\hat{S}_x + (B_{0y} + B_{sy})\hat{S}_y + (B_{0z} + B_{sz})\hat{S}_z] \\
& + d_{II} E_{tot,z} \hat{S}_z^2 - d_{\perp} E_{tot,x} (\hat{S}_x^2 + \hat{S}_y^2) + d_{\perp} E_{tot,y} (\hat{S}_x \hat{S}_y + \hat{S}_y \hat{S}_x) \\
& + M_z \hat{S}_z^2 + M_x (\hat{S}_x^2 - \hat{S}_y^2) + M_y (\hat{S}_x \hat{S}_y + \hat{S}_y \hat{S}_x) \\
& + D(T) \hat{S}_z^2
\end{aligned} \tag{1.1}$$

The components of the Hamiltonian (Eq. 1.1) indicate the vector dependence on magnetic and electric fields, and temperature, meaning their changes can be measured. Furthermore, the magnetic field vector is coupled with the spin vector, indicating that the magnetic interaction is between spin sublevels is caused by the Zeeman shift. The magnetic interaction is much stronger than the electric interaction which is caused by the Stark effect and spin-orbit coupling [13]. This strength of interaction indicates that the NV center is highly sensitive to magnetic fields, making it a perfect tool for magnetometry.

The 2D, high resolution, and wide field imaging capabilities of NV diamond make it ideal for quantum sensing. NV diamonds are capable of magnetic imaging in ambient conditions, which is crucial for keeping samples alive during biological imaging. Magnetic imaging done in ambient conditions can be performed using the Quantum Diamond Microscope (QDM). In the QDM, NV centers are present in a dense  $1.5\mu m$  layer at the top of a 4 mm x 4 mm x 1 mm NV diamond. The two common methods of growing NV diamonds are High Pressure High Temperature (HPHT) and Chemical Vapor Deposition (CVD). HPHT is the most natural formation of diamond, and uses an anvil press at 1700 K and 5 GPa to produce NV diamonds that have about 100 ppm nitrogen density [4]. CVD grows diamond substrates in single layer increments using plasma, resulting in a low ppb nitrogen density [4]. For this

study, a NV diamond grown using CVD will be used in the QDM.

## 1.2 The Quantum Diamond Microscope

A Quantum Diamond Microscope is a magnetic field imaging instrument that collects red fluorescence from an ensemble NV diamond sensor to generate a 2D, high resolution, and wide field of view magnetic field map. The NV diamond’s properties can be controlled by the QDM, making the QDM a common tool for wide-field magnetic imaging. Images of the QDM can be seen in Figure 1.5.

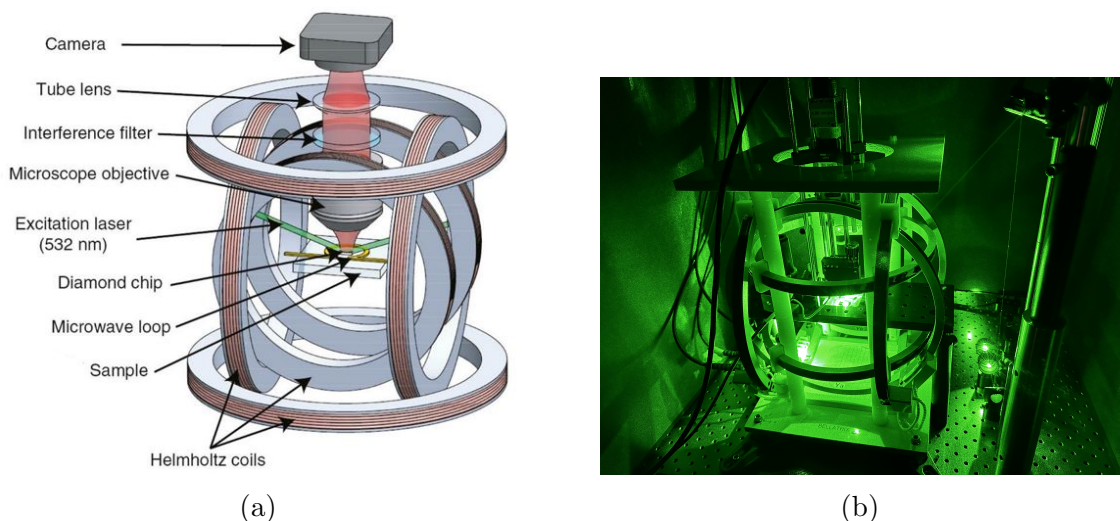


Figure 1.5: (a) QDM Graphic [10] (b) QDM in WPI’s Quantum Sensing Lab.

Key components of the QDM include the excitation laser, microwave loop, camera, and Helmholtz coils (Fig 1.5.a). The green (532 nm) excitation laser shines on the NV diamond to spin polarize the NV centers into the  $m_s = 0$  ground state at the beginning of a measurement [10]. When the laser excites NV centers from the  $m_s = 0$  ground state, they decay back to the ground state, causing the emission of red fluorescence.

The fluorescence intensity can be controlled using a MW driving field, which is sample dependent. The MW driving field is supplied to the QDM via a copper MW loop, allowing for spin-flip transitions to occur ( $m_s = 0$  to  $m_s = \pm 1$ ). The fluorescence intensity indicates the NV center’s spin sublevel because the  $m_s = \pm 1$  state emits a reduced fluorescence intensity compared to the  $m_s = 0$  state [10]. Continuous Wave (CW) ODMR is a type of measurement that probes fluorescence intensity as a function of microwave frequency. CW ODMR can perform fluorescence intensity measurements while simultaneously performing

laser pumping, and MW driving. Figure 1.6 is an example of an CW ODMR spectra that is created from QDM measurements [10]. CW ODMR is the most common technique used for QDM applications because of its easy implementation, which is why the WPI Quantum Sensing Lab uses this measurement method. Alternative approaches include pulsed ODMR and Ramsey spectroscopy [10].

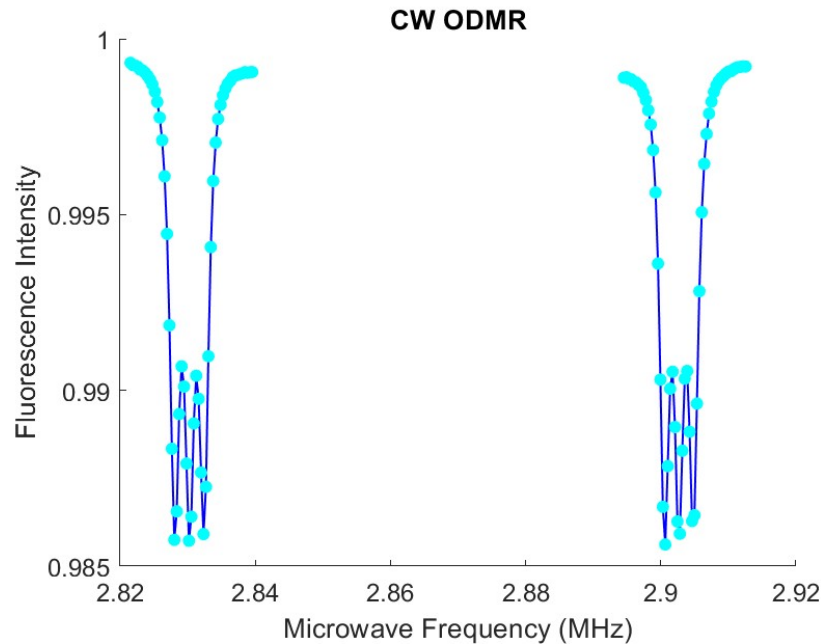


Figure 1.6: CW ODMR Spectra measuring fluorescence intensity as a function of MW frequency.

The NV diamond has four NV center orientations:  $[001]$ ,  $[111]$ ,  $[010]$ , and  $[100]$  (Fig. 1.7). The Helmholtz coils in the QDM are programmed to induce a static bias magnetic field that forces three of the NV center orientations to be degenerate ( $[001]$ ,  $[010]$ , and  $[100]$ ), leaving the NV center  $[111]$  non-degenerate [10]. This static bias magnetic field causes the Zeeman shift in the NV center's  $[111]$  ground state (Fig. 1.4). This bias magnetic field splits the  $m_s = \pm 1$  energies linearly, lifting the degeneracy between the spin sublevels. The energy differences between these sublevels is measured using ODMR spectroscopy to find the magnetic field parallel to the NV  $[111]$  quantization axis (Fig. 1.3). The QDM has three pairs of Helmholtz Coils for the x, y, and z directions. These Helmholtz coils can be programmed to be aligned or antialigned to the NV  $[111]$  orientation during magnetic imaging.

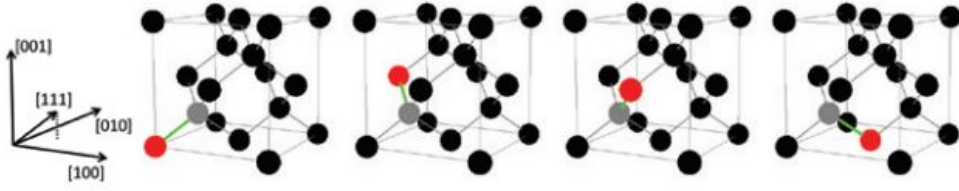


Figure 1.7: Four different NV center orientations in the diamond lattice [001], [111], [010], and [100] [10].

Finally, a camera at the top of the QDM collects fluorescence intensity from the NV diamond to generate the 2D, wide-field of view magnetic field map. A filter is placed before the camera to ensure it only collects red fluorescence. The camera measures the fluorescence intensity at each pixel. This measurement is extracted and put into an array to create a magnetic field map over an area of 1200 x 1920 pixels (Fig. 1.8) [10].

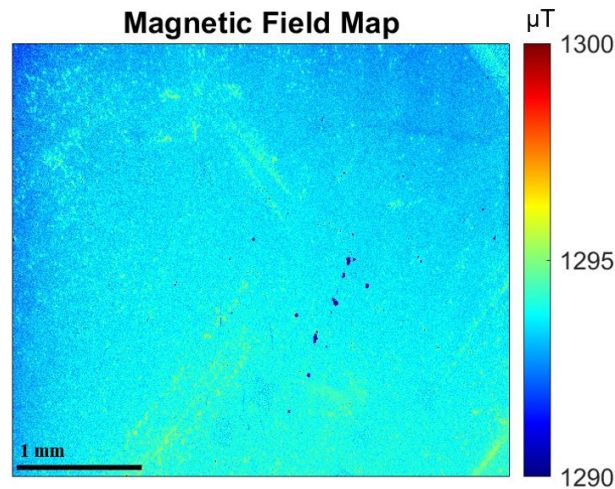


Figure 1.8: 2D, wide field of view, 1200 x 1920 pixel area magnetic field map generated using the QDM.

The QDM is an optimal sensor for magnetic imaging of SF films as compared with other magnetometers. Examples of alternative magnetic field imaging techniques are Magnetic Force Microscopy (MFM) and Superconducting Quantum Interference Device (SQUID). MFM is an Atomic Force Microscopy (AFM) technique where a magnetized tip probes magnetic fields at a high spatial resolution. MFM is only capable of probing small ( $< 100\mu m$ ) field of view (FOV) and has a DC resolution of  $> 10\mu T$  [10]. On the other hand, SQUID has high DC resolution ( $< 500\frac{fT}{\sqrt{Hz}}$ ), but its spatial resolution is limited ( $> 150\mu m$ ) [10]. The QDM overcomes the insufficiency's of these instruments. The QDM allows for 2D,

high spatial resolution, and wide-field imaging of magnetic field maps. Additionally, the QDM can operate at ambient conditions unlike SQUID which can only operate at cryogenic temperatures. This makes the QDM biocompatible because samples can be alive during measurement. The benefits of the QDM allow for it to measure a wide range of samples. Most importantly, for this work, it can image biological samples.

### 1.3 QDM Applications to Biology

The Quantum Diamond Microscope is a biocompatible quantum sensing instrument that has previously performed magnetic imaging for biological samples. Two examples include single cells and tumor tissues, both of which are tagged with magnetic nanoparticles. The QDM's high resolution and sensitivity for magnetic imaging has furthered scientific exploration.

Single-cell imaging was performed using the QDM to detect immunomagnetically labeled cells. Scientists used magnetic nanoparticles to label cancer cells to indicate the presence of the cells antigens [5]. These magnetically labels cells were put in a solution that was placed on a glass coverslip on top of the NV diamond [5]. A comparison of the fluorescence and magnetic field images indicated that the QDM was able to correctly detect and image all labeled cells (Fig. 1.9) [5]. This magnetic field image allowed scientists to determine that these cells model a spherical distribution of dipoles emitting a magnetic signal of  $3\mu T$  [5]. This was the first experiment done to image cells under ambient conditions. Additionally, this study highlighted the importance of the QDM to the future of biological imaging to help medical sciences.

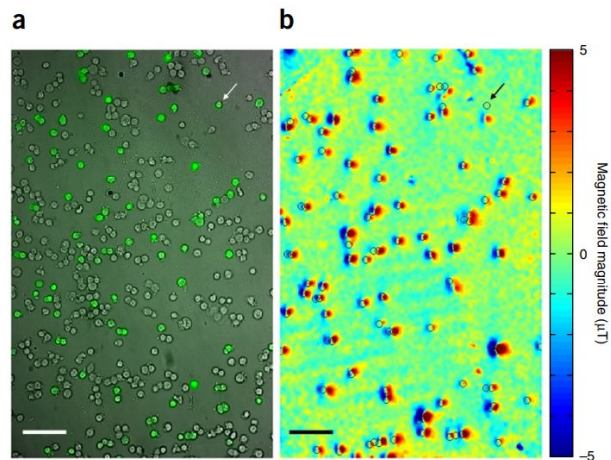


Figure 1.9: Single cell imaging using the QDM. (a) Fluorescence images of magnetically labeled cancer cells (b) magnetic field image of the magnetically labeled cancer cells [5].

The QDM has also been used to precisely image tumor tissue to improve cancer diagnoses. Scientists in this study specifically researched human lung cancer tissue. Lung cancer therapies involve the protein epidermal growth factor receptor (EGFR) [2]. Because of this, scientists magnetically labeled EGFR in a cryosection of a cancerous human lung tissue and magnetically imaged it (Fig. 1.10a) [2]. The magnetic image was compared to a simulated magnetic field map that was generated using a deep-learning algorithm (Fig. 1.10b). A comparison between these images was done to determine the accuracy of the magnetic field [5]. This comparison determined that the magnetic imaging of the tumor tissue using the QDM accurately imaged the proteins without changing the cell distribution. This experiment displayed the emerging importance the QDM has to medicine.

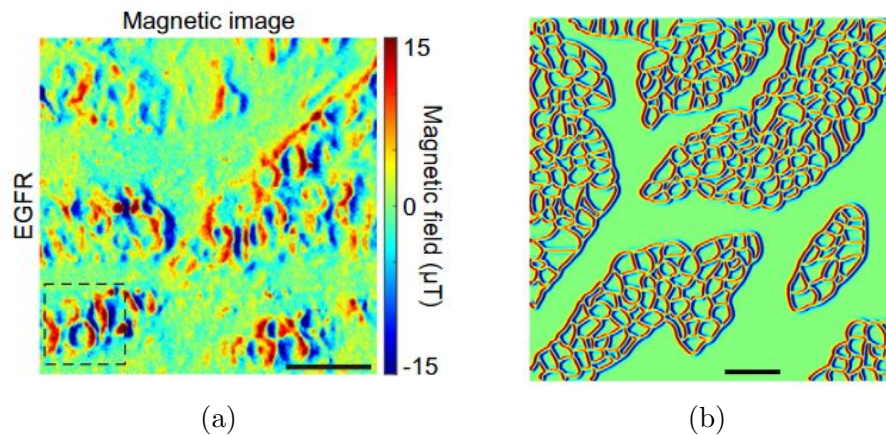


Figure 1.10: (a) Magnetic field map of human lung cancer tumor tissue, (b) simulation of tissues magnetic field map using a deep-learning algorithm [5].

These two experiments are indicative of the QDM's importance for biological magnetic imaging to further medical science. The magnetic characterization of samples from the QDM will allow for doctors and other professionals to make better conclusions about diagnoses and treatment. This will pave the way for a more refined understanding of organism processes, changing the future of medical sciences.

## 1.4 Silk Fibroin Films

Silk Fibroin (SF) films are biomaterials that are actively studied for applications to drug delivery, gene delivery, tissue, bone, and neural regeneration. An important capability of these films is their ability to be made magneto-responsive. To make SF films magneto-responsive, they are doped with magnetic particles during their growth process. Doping these

films introduces a new range of applications that is made possible by their biocompatibility, controllable biodegradability, and strong mechanical properties [6].

The biological and mechanical properties of SF films make it an important biomaterial for numerous applications. A key application of SF films is regenerative medicine. SF films are able to promote cell growth and function by reproducing properties of the extracellular matrix [8]. Moreover, SF films have a shear-thinning mechanical property which allows for their sustainability after injection into the human body [5]. The doping of magnetic nanoparticles in SF films impacts the biological and mechanical properties of these films. An important property that the magnetic nanoparticles creates is an increase in tensile strength, yield strength, elastic modulus, and elongation [8]. Furthermore, magnetic SF films have a porous structure making cell attachment and exchange of nutrients easy [8]. Additionally, the Silk Fibroin in the films can be grown to be structured or unstructured. This means that when magnetic nanoparticles are doped in structured SF films, they have distinct magnetic orientation. However, when magnetic nanoparticles are doped in unstructured silk, the film has a continuous magnetic signal throughout the sample.

The properties and previous applications of SF films indicate that it has potential to be used for spinal cord regeneration. [8]. There are currently no therapies for spinal cord regeneration. However, SF films promote cell regrowth and function, making it a promising candidate for spinal cord regeneration. It is hypothesized that placing a magneto-responsive structured SF film on a spinal cord injury, and then applying an external static magnetic field, the spinal cord will regenerate in proper alignment [6]. Spinal cords must be grown in the correction orientation to function correctly. Because of this, it is crucial to apply the correct external magnetic field during the regeneration process. To do this, first the SF films magnetic properties must be precisely determined.

The magnetic properties of SF films have mostly been characterized using SQUID; however, they have yet to be characterized using the QDM [12]. The QDM has a small sample-sensor distance, allowing for high sensitivity and resolution when generating wide field of view magnetic field maps. Additionally, the QDM is biocompatible because it can operate at ambient conditions unlike SQUID, which operates at cryogenic temperatures. The capabilities of the QDM make it an ideal instrument for studying SF films to precisely characterize their magnetic properties with high spatial resolution, which is needed for characterizing magnetically structured samples.

A key benefit of SF films is that they are able to be grown transparent. Because of this, the SF films can be placed on top of the NV diamond without obstructing the green and

red light traveling to and from the NV center. An image of the transparent SF film can be seen in Figure 1.11. Additionally, the size of the SF film is slightly larger than the NV diamond, making it easy to place on top of the diamond. This placement results in a minimal sample-sensor distance, allowing for high sensitivity and resolution magnetic imaging using the QDM. These characteristics of the SF films make it convenient to image in the QDM.



Figure 1.11: SF film on a microscope slide.

## 1.5 Goals, Motivations, and Objectives

The goal of this project was to characterize the magnetic properties of unstructured Silk Fibroin film doped in ferric chloride hexahydrate using a Quantum Diamond Microscope. The characterization of the SF films were done with the intended application being spinal cord regeneration. Based on the SF films characterization, an external, static magnetic field can be applied during spinal cord regeneration to allow for proper alignment of spinal cord growth. However, to use them for said application, it is important they are properly and precisely characterized. Emerging quantum technologies have the capabilities to characterize these materials that other technologies cannot compete with. The QDM is biocompatible and allows for 2D, high spatial resolution, wide field of view magnetic imaging, making it a perfect tool to characterize the SF films. Measuring the SF films are important because they have yet to be studied when doped in ferric chloride hexahydrate. Characterizing their magnetic properties will help scientists understand how they can be applied to spinal cord regeneration. With these goals and motivations in mind the objectives of this project are listed in the following paragraphs.

The first objective was to optimize the QDM experiment to maximize efficiency and minimize error. To make accurate conclusions about the SF films, it was first important to study the types of error associated with QDM measurements. The types of error studied were the background signal from the QDM, and the inhomogeneity from the non-uniform laser profile. By studying the overall background error signal present in QDM measurements, the optimal

imaging parameters to maximize time efficiency while still minimizing error was determined. Additionally, inhomogeneity effects the detected magnetic signal. To characterize this effect, an analysis determined the maximum area where inhomogeneity did not significantly affect the detected magnetic signal. These experiments were crucial for lowering the error signal present when imaging SF films, allowing for conclusive results about each sample.

The second objective was to demonstrate for the first time that the magnetic signal of the SF films doped in ferric chloride hexahydrate can be detected and characterized using the QDM.

The third objective was to image SF films with various concentrations of ferric chloride hexahydrate and determine how the doping concentrations affected their magnetic properties. The SF films that were measured had four different concentrations of ferric chloride hexahydrate: 0.0 mM (undoped), 0.015 mM (low), 1.50 mM (medium), and 150.0 mM (high).

## Chapter 2

# QDM Measurement Protocol and Background Signal Characterization

This chapter discusses the experiment done to fulfill the objective of optimizing the QDM experiment to minimize error in measurements. QDM imaging requires long data runs, which becomes very inefficient. Studying different aspects of the QDM imaging procedure and analysis allowed for optimized data collection parameters to be determined. To fulfill this, two experiments were conducted. The first was measuring the background noise from the QDM. The second was measuring the effect of inhomogeneity on the detected magnetic field signal.

### 2.1 QDM Measurement Protocol

The QDM employs an ensemble NV diamond where the sample of interest is placed on or near it. To image the sample of interest, it is necessary to align and then subtract each pixel measurement of the sample and NV diamond magnetic field map from the blank NV diamond magnetic field map. Because of this, it is important that the imaged NV diamond area is approximately the same for each measurement. To aid this process, the NV diamond contains etch pits which are areas of the diamond that contain no NV centers (Fig. 2.1). These etch pits are used to position the NV diamond in approximately the same spot of the camera's field of view (FOV) each time imaging is done (Fig. 2.1).

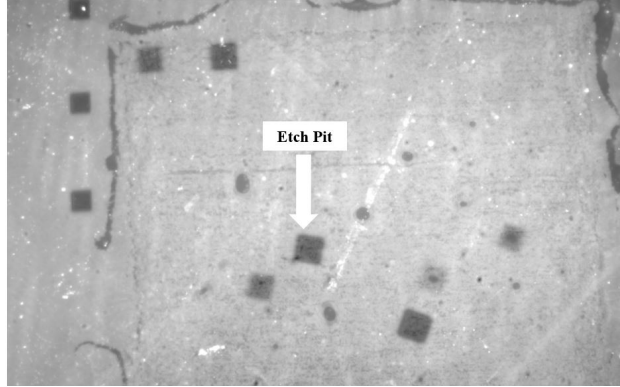


Figure 2.1: Etch pits on the NV diamond are points where there are no NV centers present. This camera FOV shows the proper NV diamond alignment using the etch pits to guide it.

After the NV diamond is properly aligned, the camera's exposure time is adjusted based on the laser power. The camera exposure time sets how much light is collected by the camera during a measurement. When a higher laser power is used the camera exposure time is set lower, and when a lower laser power is used the camera exposure time is set higher. Furthermore, it is crucial that the exposure time results in a uniform pixel saturation across the camera's FOV. Having a uniform laser profile at the proper saturation level across the NV diamond is very important when fitting the data to create magnetic field maps.

The next step for conducting a QDM measurement is applying a bias magnetic field using the Helmholtz coils. The Helmholtz coils currents are programmed to generate a static bias magnetic field aligned and antialigned along the NV diamond's [111] quantization axis. To determine the correct programming, the Biot-Savart Law calculates the x, y, and z components of the Earth's magnetic field at the exact location of the QDM. When the Helmholtz coils are properly programmed, the static bias magnetic field creates a Zeeman shift where the NV center's  $m_s = \pm 1$  states lift their degeneracy (Fig. 1.4).

The next step required for conducting a QDM measurement is programming the MW power. The MW driving field creates spin-flip transitions, allowing for the spin probability distribution to be measured via fluorescence intensity. The MW driving field is applied using a copper MW loop that surrounds the NV diamond. This loop must be close to the NV diamond's surface without touching it. The typical range for the MW power is -10 to 10 dBm. The exact value of the MW power is based on the distance between the MW loop and the NV diamond's surface. The closer the MW loop is to the diamond surface, the lower the MW power will be. The MW loop distance from the NV diamond can be adjusted manually, so it is crucial to test the optimal MW power for each experiment. The ODMR spectra is used to determine the optimal MW power because the graph will give a low amplitude and a

distinct contrast between the peaks of each resonance dip (Fig. 2.2).

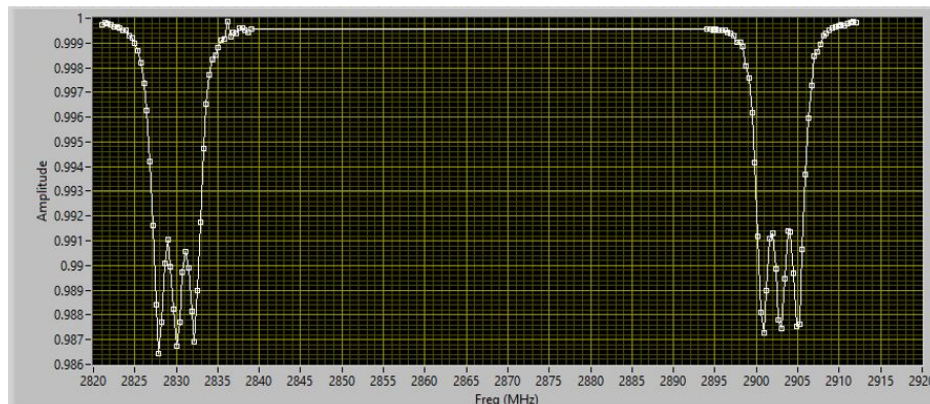


Figure 2.2: Example ODMR spectrum averaged over all camera pixels.

Adjusting these key parameters generates an accurate magnetic field map from a QDM measurement. A Graphics Processing Tool (GPU) in MATLAB is used for primary analysis to generate the magnetic field map. This GPU fit models three Lorentzian line shapes on the two resonance fits in the ODMR spectra to generate a 1200 x 1920 pixel area magnetic field map (Fig. 1.7). The average and standard deviation of each pixel measurement in the magnetic field map is calculated to measure the magnetic signal and associated error.

## 2.2 QDM Background Noise

Long data runs are needed to reduce error signal from QDM measurements. However, there is a point of diminishing return where longer data runs doesn't significantly reduce error signal. Therefore, to efficiently take data a measurement of QDM background noise determined the optimal experimental run time. This was crucial for measuring SF films in the QDM. SF films burn under high laser power after an extended period of time; therefore, it was important to determine the optimal experimental run time that minimized data collection time and detected magnetic error signal.

To determine the optimal experimental run time, a study was done to measure the background magnetic error signal from the QDM. An experiment was designed that measured the magnetic field error signal from a blank NV diamond over a run time range of 2-24 hours in 2hr increments. For each run time the same QDM parameters were used to ensure the independent variable was run time. These parameters were a laser power of 3.00 W, exposure time of 0.73  $\mu$ s, and microwave power of -8 dBm. For each run time two magnetic field maps of the blank NV diamond were taken: Aligned [111] and Antialigned [111]. After

each magnetic field map was collected, they were first analyzed in MATLAB using a GPU fit. This generated the initial magnetic field map and signal. Next, a secondary MATLAB data analysis was run to correct the magnetic field map by removing over and undersaturated (hot) pixels. To remove these hot pixels, the lower bound for the pixel intensity was set to 150 out of a maximum value of 255. All pixels that had an intensity lower than 150 were “removed” from the magnetic field map. These hot pixels are represented by dark blue spots on the magnetic field map. Removing these pixels generated a corrected magnetic field map for each run time which corresponded to an accurate representation of the standard deviation error signal at each run time. The corrected magnetic field maps for 2hr, 12hr, and 24hr Aligned [111] can be seen in Figure 2.3.

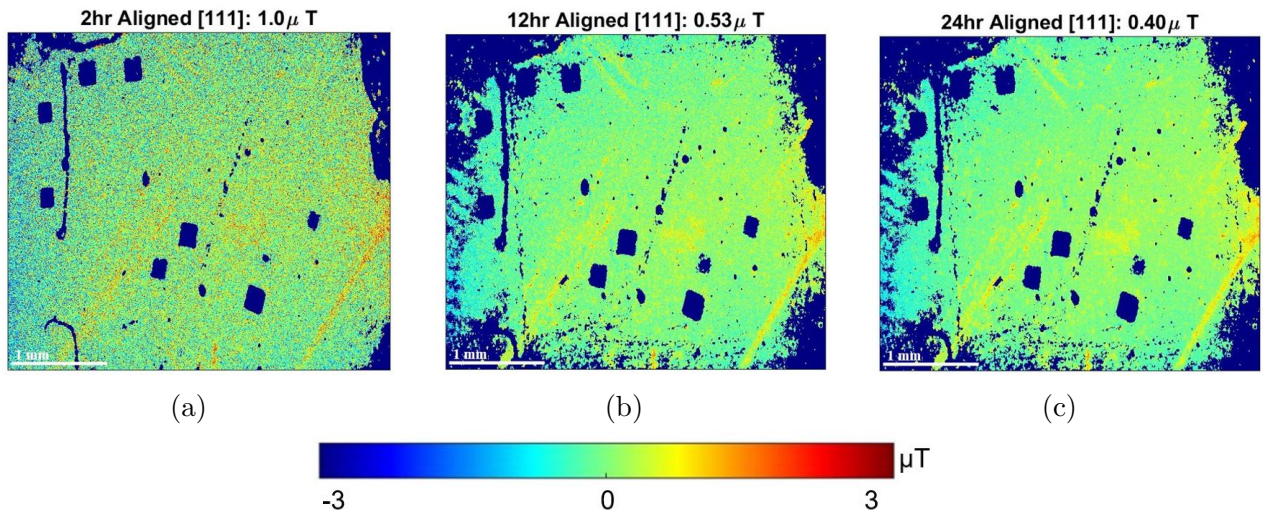


Figure 2.3: Corrected magnetic field maps with their associated magnetic error signal (a)2hr Aligned [111] with an error signal of  $1.0\mu T$ , (b)12hr Aligned [111] with an error signal of  $0.53\mu T$ , (c) 24hr Aligned [111] with an error signal of  $0.40\mu T$ .

The magnetic field maps in Figure 2.3 have a distinct decrease in error signal as experimental run time increases. However, the 12 hr and 24 hr run times have a small error signal difference compared to the difference between 2 hr and 12 hr. Because of this, it can be concluded that there is a point between 12 and 24 hrs where taking data for longer doesn’t significantly reduce the error signal.

The magnetic error signal from each blank NV diamond’s magnetic field map for the 2-24 hr run times was recorded. MATLAB was used to create a figure of merit which was a graph of the magnetic signal’s standard deviation ( $\mu T$ ) versus measurement time (hr) (Fig. 2.4). This figure was fitted with an exponential function to give an estimate for the approximate

error signal at each run time. From analyzing the graph and its associated fit, the optimal experimental run time was determined.

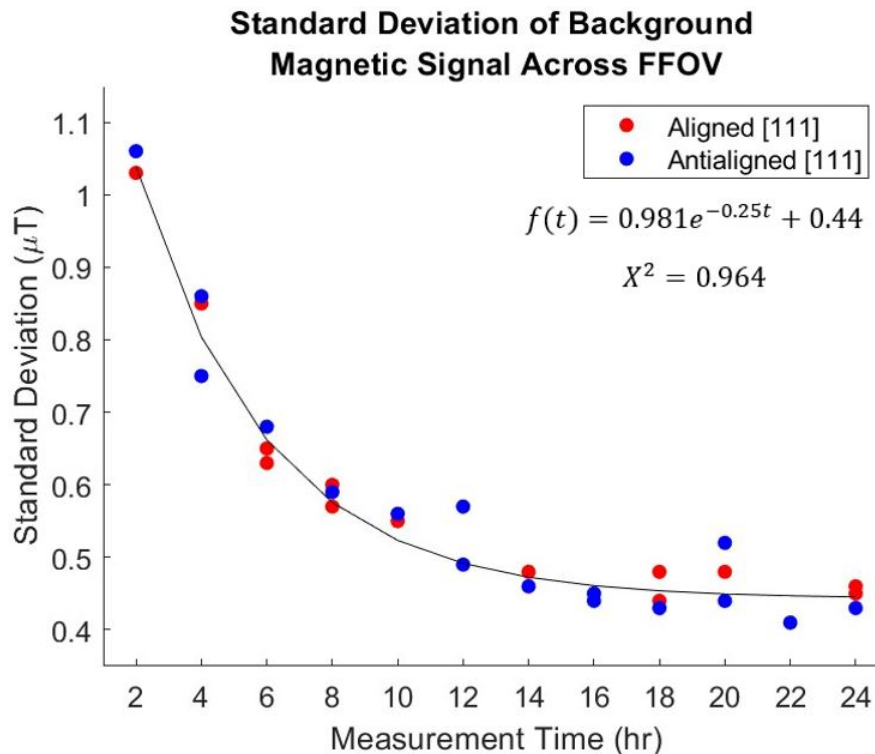


Figure 2.4: Magnetic field standard deviation ( $\mu T$ ) vs. measurement time (hr). The standard deviation from the Aligned [111] is red, and the Antialigned [111] is blue. The data is fitted with the exponential function  $f(t) = 0.981e^{-0.25t} + 0.44$  with  $X^2 = 0.964$ .

In Figure 2.4, the error significantly decreased after 4–10-hour data collection. Therefore, taking data for less than 10 hours is not effective because there is a high error signal after pixel removal. The run times in the range of 16–24 hours have similar error signal, so taking data for more than 24 hours is not effective. Therefore, the optimal experimental run time was a range of 10–16 hours. Magnetic images of SF films in the QDM were collected for ten hours; however, the error signal was further reduced by studying the effect of inhomogeneity on the magnetic signal.

## 2.3 QDM Inhomogeneity

To further understand the error signals from QDM measurements, a study was done to characterize the inhomogeneity on the NV diamond and its affect on detected magnetic signal. Inhomogeneity is caused by a non-uniform laser profile over the NV diamond, which

creates different levels of laser saturation across the NV diamond. This inhomogeneity is shown in Figure 2.5, where there is a brighter grey towards the center, but darker grey at the edges of the image. The QDM uses a Gaussian beam that has a small spot diameter relative to the full area of the diamond. This creates the non-uniform laser profile across the NV diamond. The non-uniform saturation, results in different detected magnetic signals throughout the magnetic field map. To characterize the effect of the inhomogeneity, this study determined the maximum area that could be analyzed where a uniform laser profile was largely present, resulting in a uniform magnetic signal across the magnetic field map.

To characterize the inhomogeneity, subsections from magnetic field maps taken in Chapter 2.2 were analyzed. The subsections were created around the center point of the Gaussian beam spot at (500,1300) pixel. Six subsections of increasing area surrounding the center point were created and analyzed. Increasing the subsection area allowed for a conclusion of the maximum area that could be analyzed before inhomogeneity significantly affected the detected magnetic signal. The subsection areas that were measured can be seen in Figure 2.5. For each subsection area, a MATLAB code generated their magnetic field map and determined their magnetic signal and standard deviation. The subsection magnetic field maps for the 2hr, 12hr, and 24hr aligned [111] measurements are shown in Figures 2.6, 2.7, and 2.8 respectively.

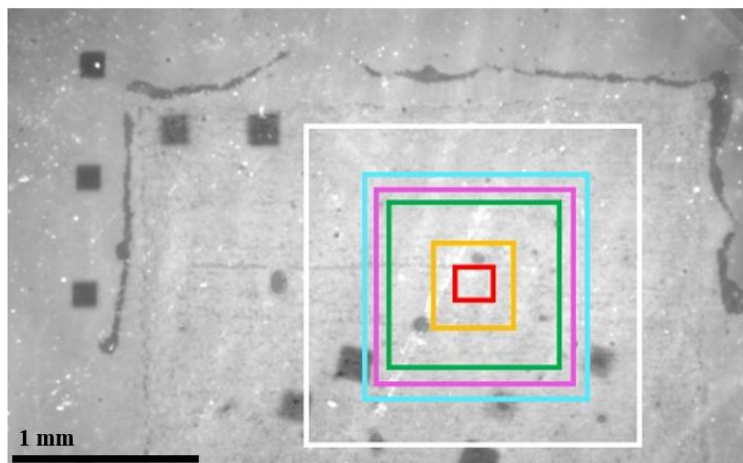


Figure 2.5: Optical image showing the non-uniform laser profile over the NV diamond. Subsection areas that were analyzed are outlined. Red is the 50x50 pixel area, yellow is the 100x100 pixel area, green is the 300x300 pixel area, purple is the 350x350 pixel area, blue is the 400x400 pixel area, and white is the 600x600 pixel area.

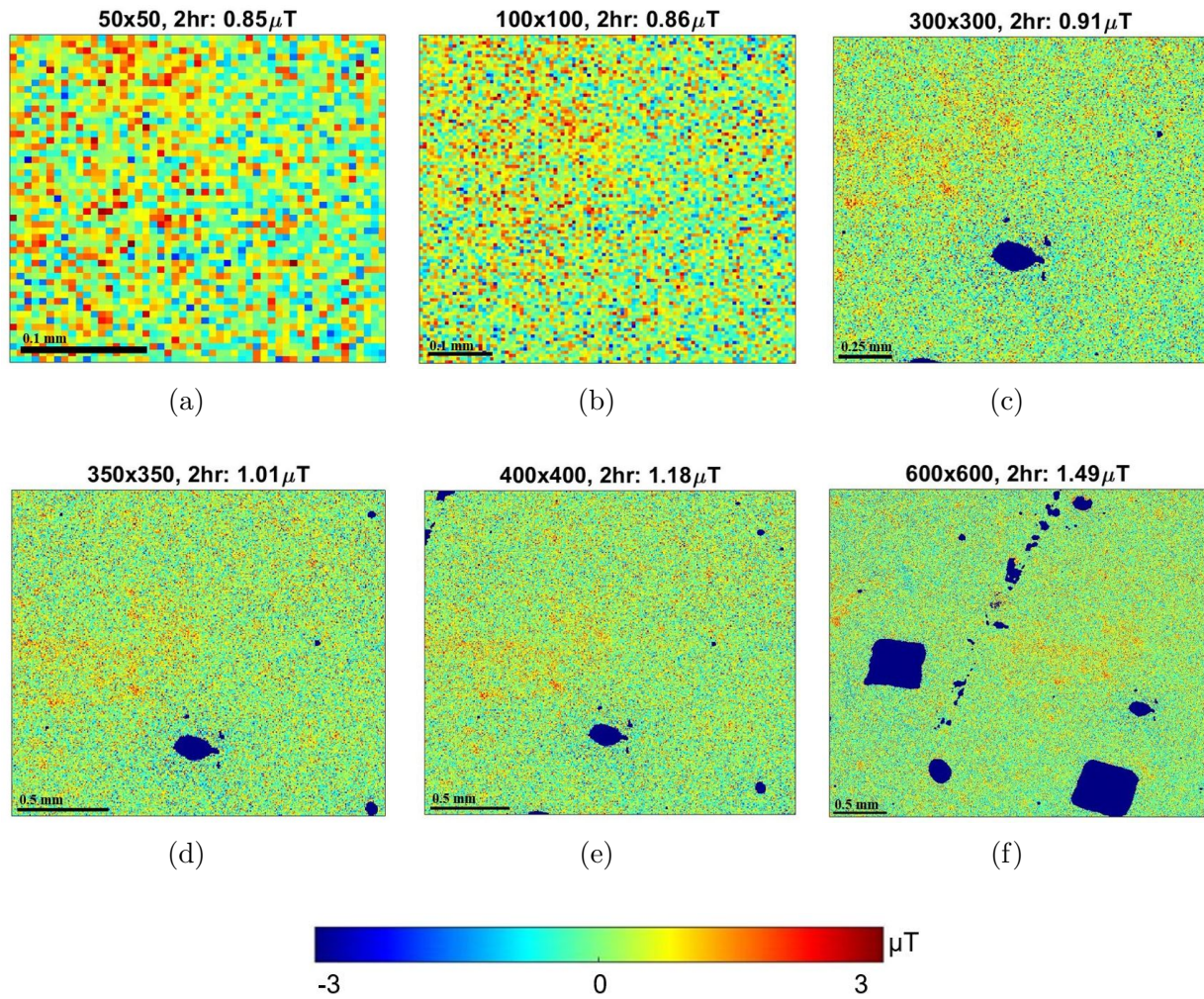


Figure 2.6: 2hr aligned [111] subsection magnetic field maps and their error signal. (a) 50x50 pixel area (b) 100x100 pixel area (c) 300x300 pixel area (d) 350x350 pixel area (e) 400x400 pixel area (f) 600x600 pixel area.

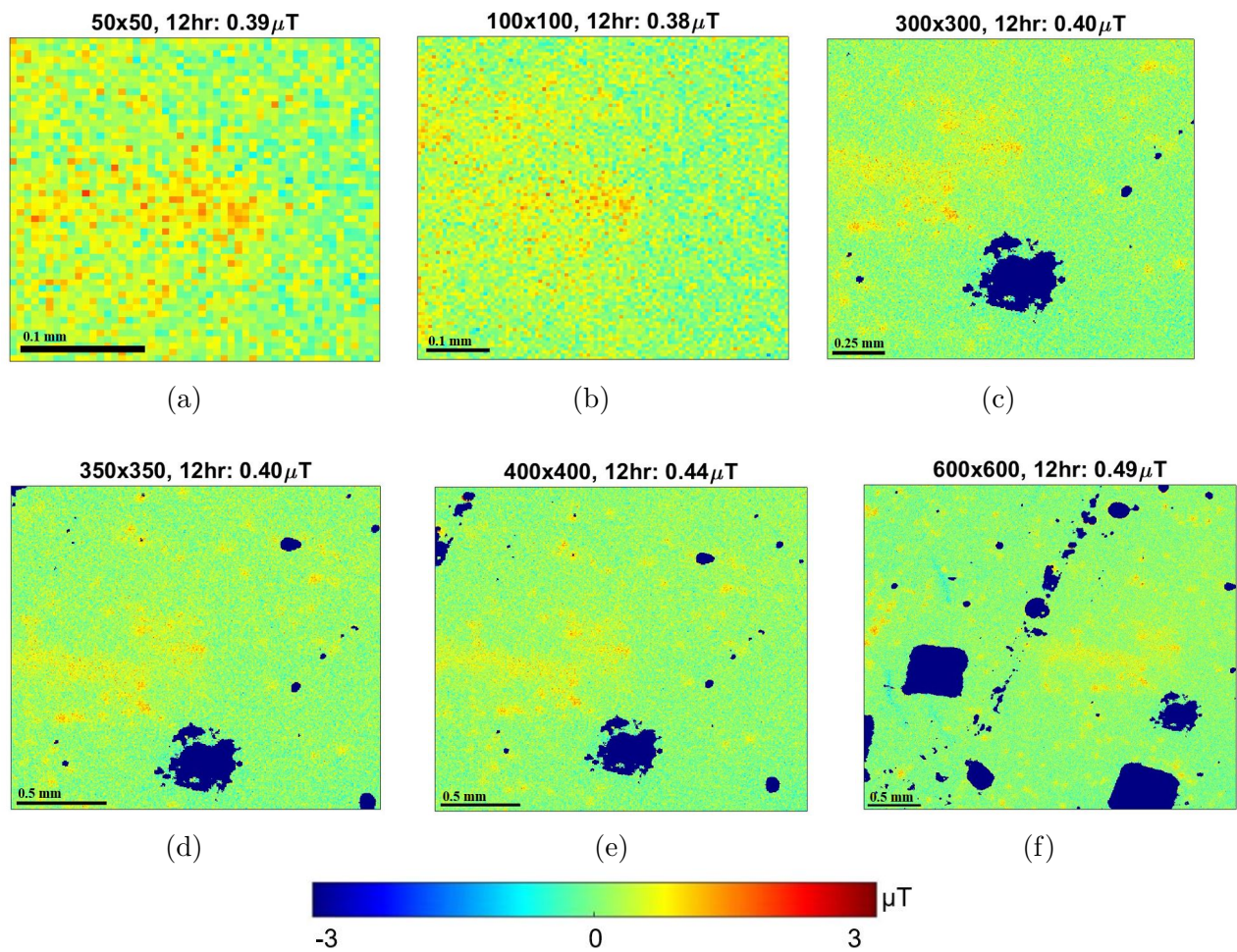


Figure 2.7: 12hr aligned [111] subsection magnetic field maps and their error signal. (a) 50x50 pixel area (b) 100x100 pixel area (c) 300x300 pixel area (d) 350x350 pixel area (e) 400x400 pixel area (f) 600x600 pixel area.

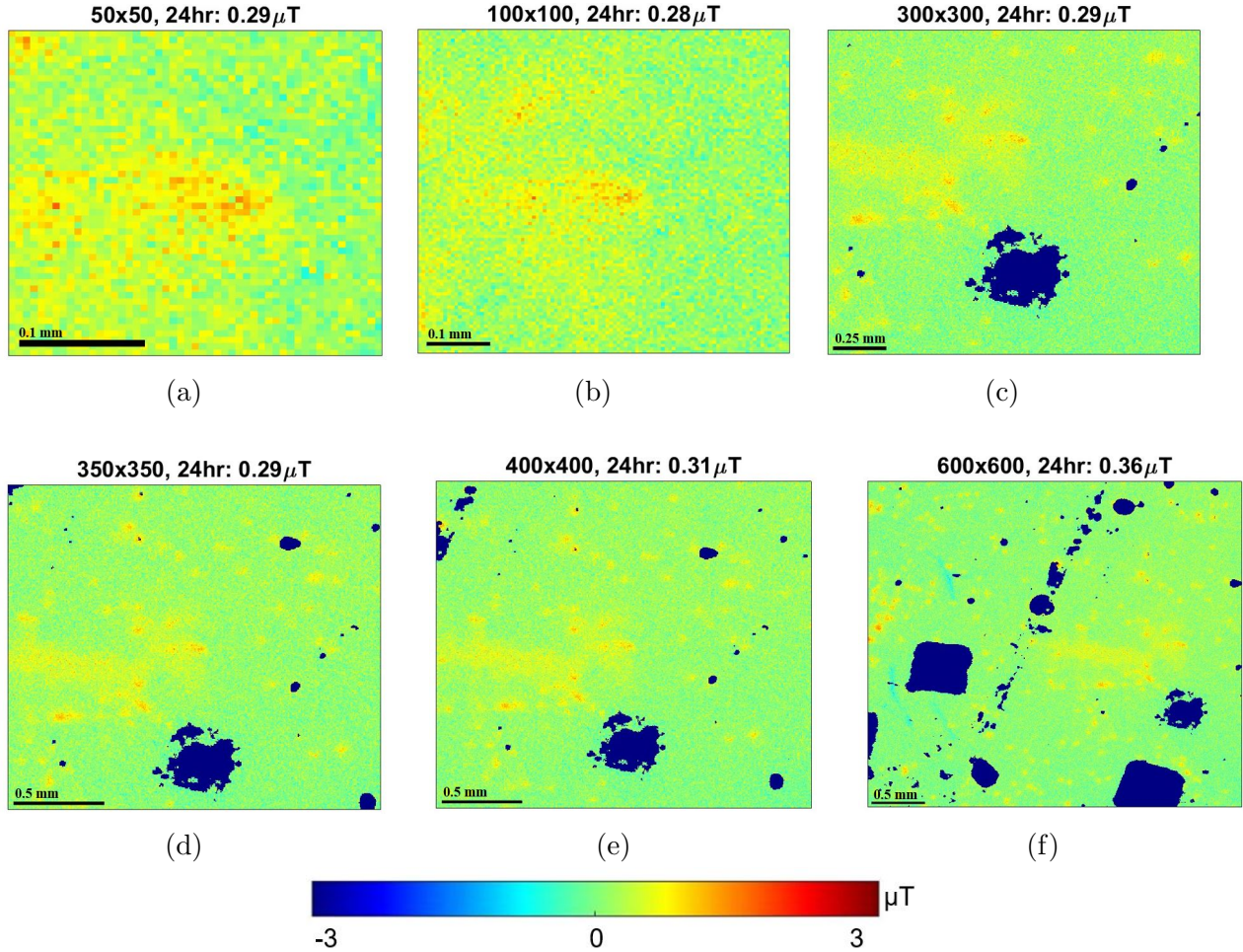


Figure 2.8: 24hr aligned [111] subsection magnetic field maps and their error signal. (a) 50x50 pixel area (b) 100x100 pixel area (c) 300x300 pixel area (d) 350x350 pixel area (e) 400x400 pixel area (f) 600x600 pixel area.

The error signal significantly increased around the 400 x 400 pixel area subsection for each run time; therefore, inhomogeneity becomes significant at areas equal to or larger than 400 x 400 pixels. All subsection magnetic field maps had lower error signal than the full field of view magnetic field maps from Figure 2.3 when the area was less than 400 x 400 pixels. In conclusion, subsection analysis is important to reduce the detected magnetic error signal, allowing for accurate conclusion to be made about samples magnetic properties. Overall, the best subsection area to analyze was the 300 x 300 pixel area because it maximized pixel area while minimizing error.

This study of inhomogeneity was also compared to Federico Poggioni's study of QDM error signal in the MQP "Construction and Characterization of a Quantum Diamond Microscope"

completed in 2021 [11]. This comparison was done to determine how the physical setup of the QDM also affects the error signal present. During Federico’s MQP the QDM was on an optics breadboard on a desk, whereas for this work, the QDM was on an optics table. It is hypothesized that the QDM on an optics table is more stable, thus has lower error than the breadboard setup. For Federico’s 2hr measurement, an area of 135 x 95 pixels was analyzed. This analysis measured an error signal of  $0.99\mu T$  [11]. Using the data from Chapter 2.2, the 2hr magnetic field map was analyzed over a 135 x 95 pixel area. This analysis measured an error signal of  $0.86\mu T$ . This analysis had a smaller error compared to the 2021 measurement, confirming that an optics table is important for stabilizing the experiment to lower the detected background error signal.

The characterization of inhomogeneity concluded that the uniformity of the laser profile plays a key factor in the magnetic signal detected from QDM measurements. Another possible source of inhomogeneity that was not studied is strain defects in the NV diamond. The NV diamond had intrinsic stress, called strain defects, which shift the NV center’s resonant frequencies, affecting the spins dephasing time [9]. There are four major types of strain features: large-scale plastic deformation, dislocation bundle, isolated dislocation, and x-defect. Most of these deformations are due to dislocations that form on the crystal during homoepitaxial growth [9]. The strain in the diamond limits the NV diamonds sensitivity during measurement and affects ODMR spectra fitting. These effects create inhomogeneity in magnetic field maps produced from QDM measurements.

To improve future studies a Top Hat beam can be used to create a uniform laser profile over the NV diamond. This would make the detected magnetic signal more homogeneous across the full magnetic field map. Another important future study would be creating a code that sweeps the magnetic field map to find subsections that best maximize the pixel area while minimizing the error. This code would increase efficiency during the subsection analysis process. Additionally, the analysis of measuring error from the QDM was done using a laser power of 3.00 W. To create a more in-depth figure of merit, as shown in Figure 2.4, an important future study would be to study the background error signal at various laser powers. Not all experiments use 3.00 W laser power; therefore, performing this study would give an accurate representation of the error signal associated at each measurement run time. From this data the optimal experimental run time for each laser power could be determined, creating better QDM optimization.

# Chapter 3

## Measuring Silk Fibroin Films

This chapter discusses magnetic imaging the Silk Fibroin (SF) films doped in ferric chloride hexahydrate in the QDM to characterize their magnetic properties. These experiments measured Silk Fibroin films doped in four different concentrations of ferric chloride hexahydrate: 0.00mM (undoped), 0.015mM (low), 1.50mM (medium), and 150.0mM (high). In addition to detecting the magnetic signal from each sample, their ferromagnetic and paramagnetic components were measured. Characterizing each SF films magnetic properties is crucial to understand their application for spinal cord regeneration.

### 3.1 Sample Preparation and Imaging Procedure

SF films are a thin biological sample prone to burning under high laser power for an extended period of time (Fig. 3.1). Additionally, different concentrations of ferric chloride hexahydrate in the samples affect the upper boundary of laser irradiance and time for sample imaging. Because of this, it was important to study the parameters, including sample placement, optimal laser power, and measurement time, required to image the four sample concentrations.

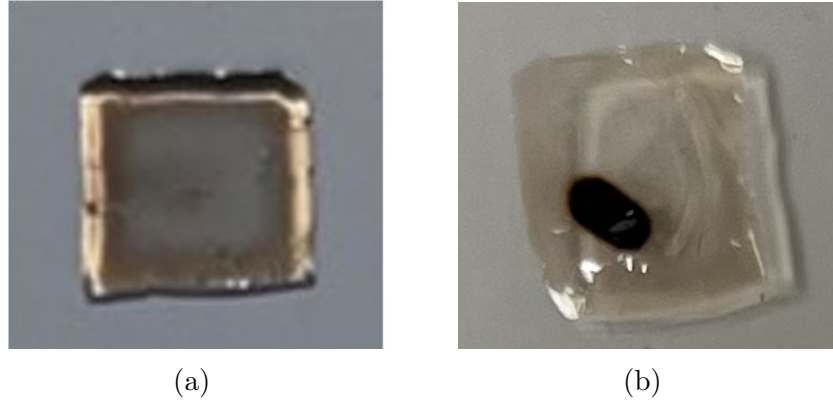


Figure 3.1: SF film (a) unburned, (b) burned.

The first test was determining how to place the SF films in the QDM with the NV diamond for imaging. The closer the sample is to the NV diamond, the higher the sensitivity and spatial resolution of the magnetic field map [10]. Figure 3.1 shows that the SF films are a transparent sample, allowing them to be placed on top of the NV diamond. The samples transparency does not obstruct the green laser traveling to the NV diamond, nor the red fluorescence traveling to the camera. Additionally, it was important that the copper microwave loop surrounded the sample and the diamond without touching it. This setup can be seen in Figure 3.2.

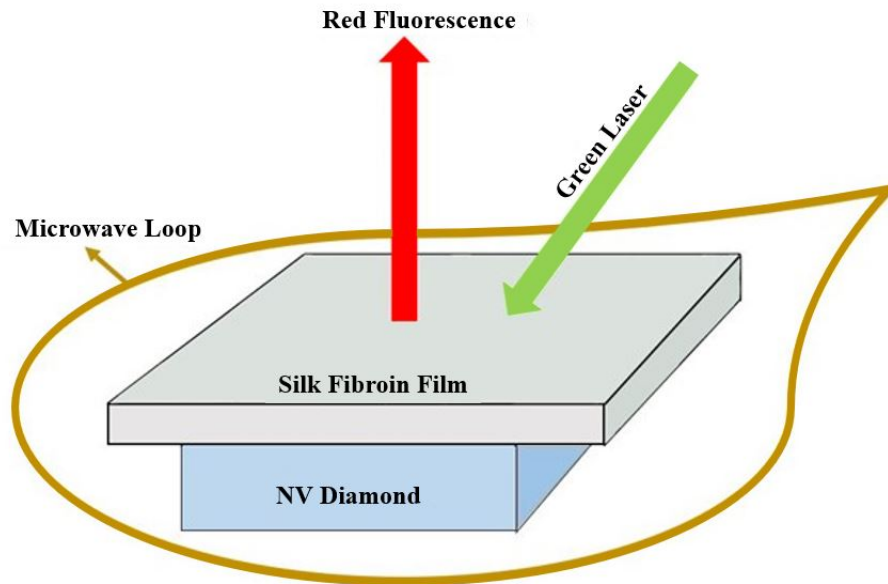


Figure 3.2: Setup of the transparent SF film sample on the NV diamond.

Next, to study the optimal laser power and run time, heat testing experiments were done

for each sample. Each sample was placed in the QDM with no NV diamond present. Next, a laser power range of 0.5-2.00W was tested, where each new heat test increased the laser power by 0.5 W in this range. During testing, the sample was checked every 15 minutes until it burned. The optimal parameters for laser power and run time are recorded in Table 3.1. These optimal values were used to image the samples in the QDM to characterize their magnetic properties.

Table 3.1: Optimal laser power (W) and run time (hr) for each SF film sample.

<b>SF Film Concentration (mM)</b>	<b>Laser Power (W)</b>	<b>Run Time (hr)</b>
0.00	2.00+	10+
0.015	2.00+	10+
1.50	1.50	10
150.0	1.00	10

The final test done was determining how the SF films affected the cleanliness of the NV diamond. Because the SF Films are doped with ferric chloride hexahydrate, they leave magnetic residue on the NV diamond after imaging. When imaging the blank NV diamond after the sample, there was magnetic residue from the sample on it. This results in an inaccurate representation of the blank NV diamond magnetic signal, thus affecting the magnetic signal measured from the sample. To counteract this, sulfuric acid was used to thoroughly clean the NV diamond after sample imaging.

Based on the experiments that determined how to image SF films in the QDM, an overall imaging procedure for the SF films in the QDM was created. The first step was to perform the acid cleaning of the NV diamond. Then, blank images of the NV diamond in the aligned and antialigned [111] directions were measured. For each image, a GPU fit was done to generate the initial magnetic field map and signal from the blank NV diamond. Following blank NV diamond imaging, the SF film samples were placed on top of the NV diamond and imaged in the aligned and antialigned [111] directions. Again, primary analysis was done to generate the initial magnetic field map and signal of the sample and NV diamond together. For the secondary analysis, the pixels of the sample and blank magnetic field maps were aligned and then subtracted to get the magnetic field map of the SF film alone (Fig. 3.3).

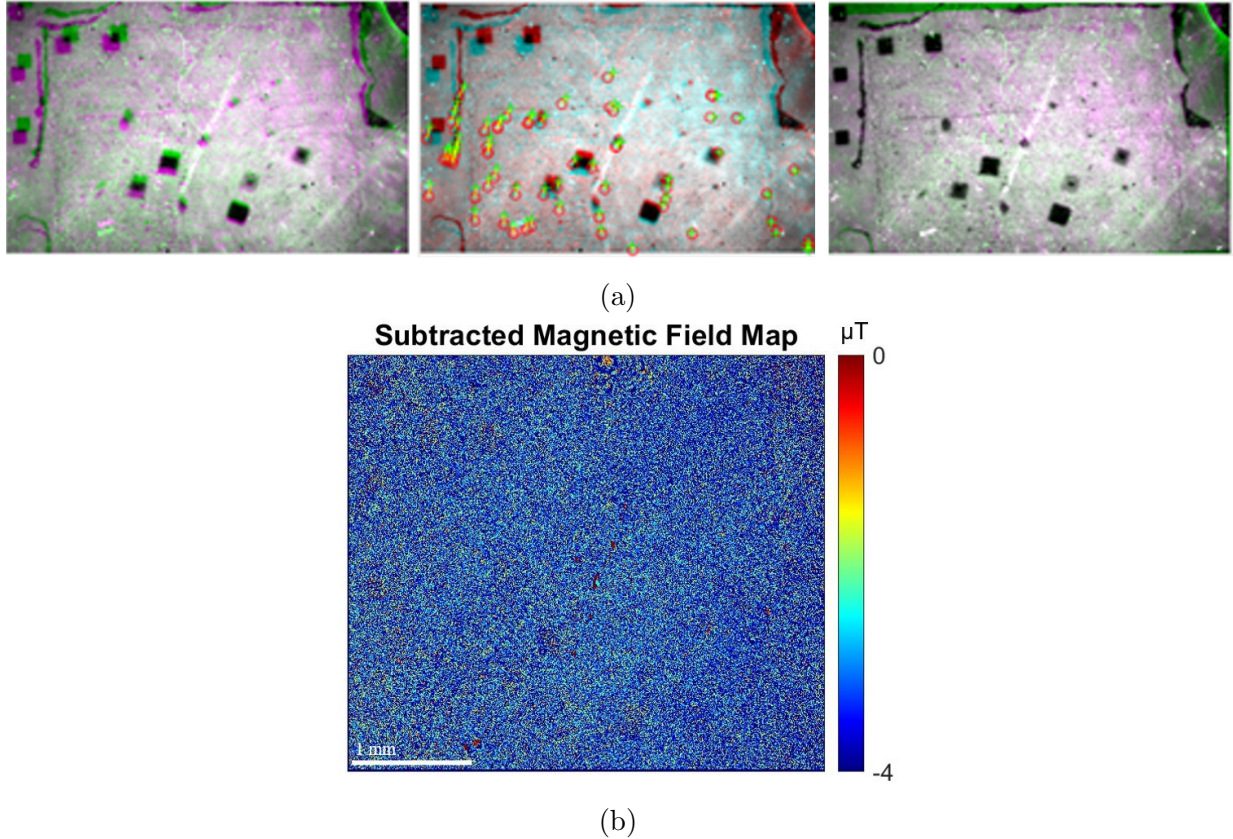


Figure 3.3: (a) Alignment of sample and blank pixels (b) Example of subtracted magnetic field map.

After subtraction, the final step of the data analysis was removing the hot pixels from the samples magnetic field map. This procedure created an accurate sample magnetic field map for measuring SF films magnetic signal.

## 3.2 Measurements of the SF Film Magnetic Signal

To study the effect of ferric chloride hexahydrate on the samples magnetic signal, four SF films with varying concentrations of ferric chloride hexahydrate were measured in the QDM. The sample concentrations were 0.00 mM (undoped), 0.015 mM (low), 1.50 mM (medium), and 150.0 mM (high). The first experiment performed was magnetic imaging of each sample at their optimal laser power and run time (Table 3.1). The magnetic field maps were corrected to have hot pixels removed, with the boundary being where the error was lowest. To minimize the error in magnetic signal due to inhomogeneity across the wide 1200 x 1920 pixel field of view, subsection analysis was done on the magnetic field maps. A 300 x 300 pixel area was analyzed, which was the maximum area where magnetic signal

is not significantly affected by inhomogeneity. The average magnetic signal and standard deviation was calculated for the 300x300 magnetic field map. The measurement results for each sample and the associated bias magnetic field direction are shown in Fig.3.4.

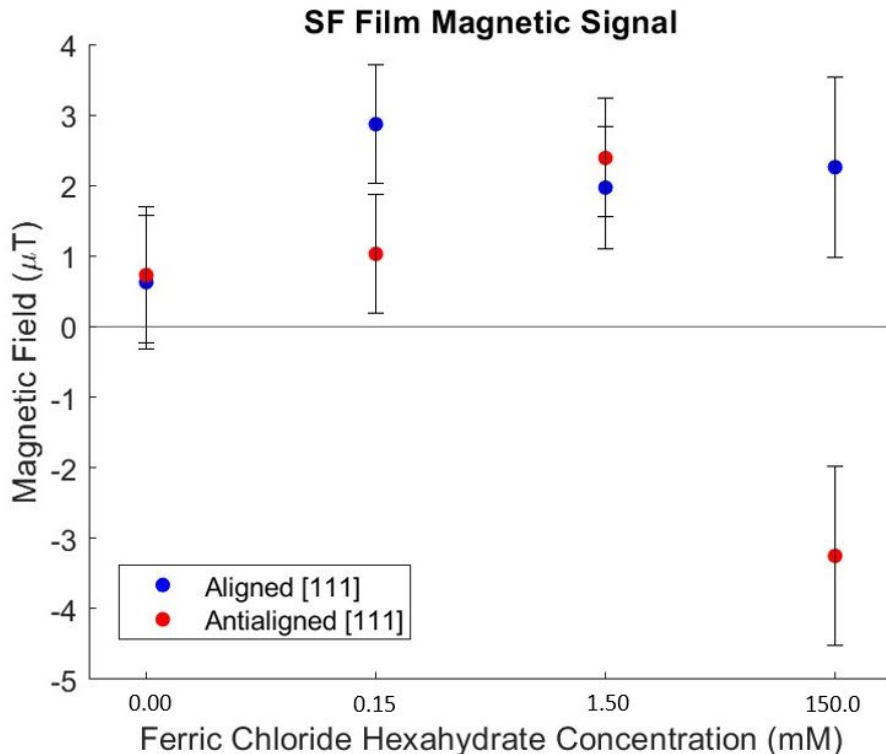


Figure 3.4: Magnetic signal of SF film samples from 300x300 magnetic field maps. The blue dot is the antialigned [111] measurement, and the red dot is the aligned [111] measurement.

The higher the ferric chloride hexahydrate concentration, the greater the samples magnetic signal. The aligned [111] magnetic signal for the undoped sample was  $0.63 \pm 0.94\mu T$ , low sample was  $2.87 \pm 0.84\mu T$ , medium sample was  $1.97 \pm 0.86\mu T$ , and the high sample was  $2.26 \pm 1.28\mu T$ . The antialigned [111] magnetic field signal for the undoped sample was  $0.73 \pm 0.96\mu T$ , low sample was  $1.03 \pm 0.84\mu T$ , medium sample was  $2.39 \pm 0.84\mu T$ , and the high sample was  $-3.25 \pm 1.27\mu T$ . The error bars represent the standard deviation across the selected area, which is can be due to both the experimental inhomogeneity and the variation of the sample.

To further characterize the magnetic properties of the SF films, their paramagnetic and ferromagnetic components were calculated and graphed in Figure 3.5. Paramagnetic means the sample needs and external magnetic field to be magnetic. Ferromagnetic means the sample is intrinsically magnetic. Comparing the magnetic signal in the aligned and antialigned

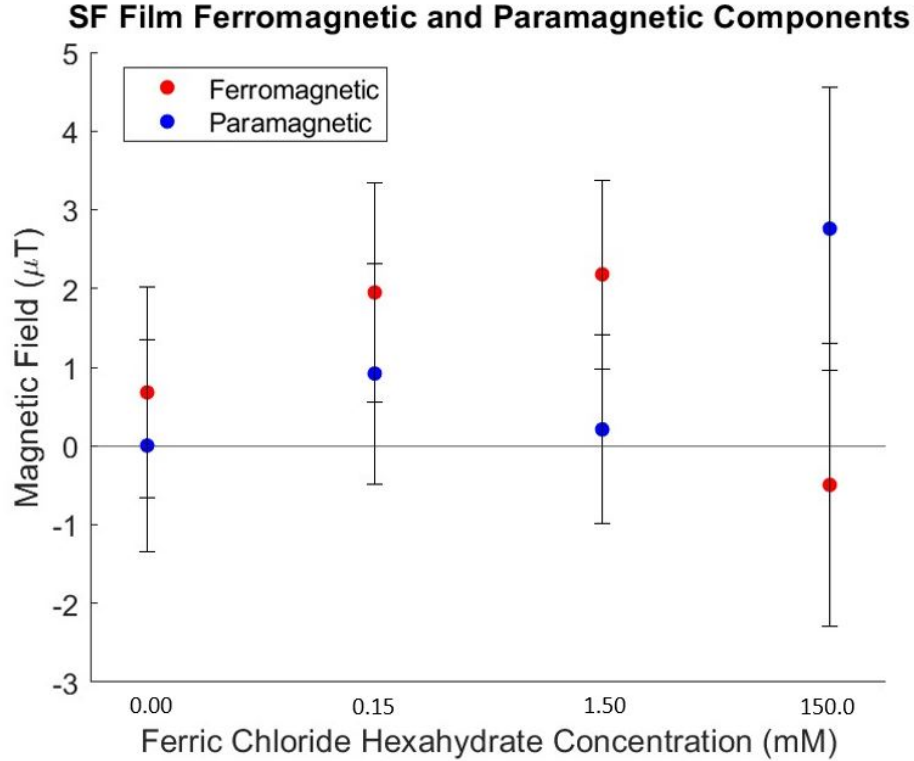


Figure 3.5: Paramagnetic and ferromagnetic signal from each SF Film samples. The red dot is ferromagnetic measurement, and the blue dot is the paramagnetic measurement.

[111] external magnetic field conditions, the ferromagnetic and paramagnetic behaviour was calculated by averaging either the difference or sum of the magnetic signal in both experiments respectively. Figure 3.5 indicates that the higher the ferric chloride hexahydrate concentration is, the more paramagnetic the sample is. The paramagnetic signal of the undoped sample is  $0.005 \pm 1.34 \mu T$ , whereas the paramagnetic signal of the high sample is  $2.76 \pm 1.8 \mu T$ . Characterizing this property was crucial for future studies done with SF films to determine how they could be applied to spinal cord regeneration with tuned magnetic properties.

This experiment proved that it was possible to image biomaterials in the QDM for the first time. The research done here will set the foundation for future research done to image biomaterials in the QDM. Additionally, SF films doped in ferric chloride hexahydrate were studied for the first time in this experiment. Furthermore, this research shows that it is possible to engineer the magnetic properties of SF films by adjusting the ferric chloride hexahydrate concentration, which can allow them to be tailored for applications such as spinal cord regeneration therapy.

# Chapter 4

## Conclusions and Future Work

This work experimentally demonstrated that the QDM can be used for magnetic imaging of biomaterials. More specifically, a QDM was used for the first time to successfully image and characterize the magnetic properties of SF films doped in ferric chloride hexahydrate. The measurements showed that a higher ferric chloride hexahydrate concentration results in larger magnetic signal and gives rise to more paramagnetic behavior. Ferric chloride hexahydrate is a nontoxic chemical compound to humans; therefore, it is safe to use for spinal cord regeneration. The methods developed in this work can be used for future studies of SF film magnetic imaging. The characterization of these samples will allow for doctors and other scientists to better understand how to apply and tune SF films to spinal cord regeneration, resulting in its first proven therapy method.

An important future step is to demonstrate magnetic imaging of structured SF films. In this work, nonstructured SF films were studied to learn if biomaterials could be studied in the QDM, and to determine if a magnetic signal could be detected. However, structured SF films would be needed for proper application to spinal cord regeneration. Structured SF films contains silk fiber fragments. When these SF films are doped with magnetic nanoparticles, the samples develop directionally oriented magnetic properties, and an external magnetic can then be used to align all of the silk fibers in the same desired direction. This characteristic would allow for spinal cords to regenerate with correct alignment.

To further develop the QDM for studying a SF films, it is important to mitigate undesirable sample heating during measurements. SF films are susceptible to burning under high laser power, which is needed to achieve higher magnetic sensitivity. Designing and building a sample specific mount or sample holder to mitigate the heating effects on the sample would allow for imaging at high laser power for longer time. Mount materials and any passive or

active cooling systems need to be considered to ensure they are compatible with the QDM. Additionally, allowing for the use of Total Internal Reflection (TIR) during magnetic field measurements through the addition of a glass prism underneath the NV diamond would trap the laser light in the diamond, minimizing the laser illumination on the samples.

This research experimentally demonstrated magnetic imaging of SF films with an NV diamond quantum sensor. Furthermore, it paved the way for future experimental improvements to the QDM, and further studies of various SF films.

# Bibliography

- [1] Gopalakrishnan Balasubramanian, Andrii Lazarev, Sri Ranjini Arumugam, and Deyuan Duan. Nitrogen-Vacancy color center in diamond—emerging nanoscale applications in bioimaging and biosensing. *Current Opinion in Chemical Biology*, 20:69–77, June 2014.
- [2] Sanyou Chen, Wanhe Li, Xiaohu Zheng, Pei Yu, Pengfei Wang, Ziting Sun, Yao Xu, Defeng Jiao, Xiangyu Ye, Mingcheng Cai, Mengze Shen, Mengqi Wang, Qi Zhang, Fei Kong, Ya Wang, Jie He, Haiming Wei, Fazhan Shi, and Jiangfeng Du. Immuno-magnetic microscopy of tumor tissues using quantum sensors in diamond. *Proceedings of the National Academy of Sciences*, 119(5):e2118876119, February 2022. Publisher: Proceedings of the National Academy of Sciences.
- [3] C.L. Degen, F. Reinhard, and P. Cappellaro. Quantum sensing. *Reviews of Modern Physics*, 89(3):035002, July 2017. Publisher: American Physical Society.
- [4] Andrew M. Edmonds, Connor A. Hart, Matthew J. Turner, Pierre-Olivier Colard, Jennifer M. Schloss, Kevin S. Olsson, Raisa Trubko, Matthew L. Markham, Adam Rathmill, Ben Horne-Smith, Wilbur Lew, Arul Manickam, Scott Bruce, Peter G. Kaup, Jon C. Russo, Michael J. DiMario, Joseph T. South, Jay T. Hansen, Daniel J. Twitchen, and Ronald L. Walsworth. Characterisation of CVD diamond with high concentrations of nitrogen for magnetic-field sensing applications. *Materials for Quantum Technology*, 1(2):025001, March 2021. Publisher: IOP Publishing.
- [5] David R. Glenn, Kyunghoon Lee, Hongkun Park, Ralph Weissleder, Amir Yacoby, Mikhail D. Lukin, Hakho Lee, Ronald L. Walsworth, and Colin B. Connolly. Single-cell magnetic imaging using a quantum diamond microscope. *Nature Methods*, 12(8):736–738, August 2015. Number: 8 Publisher: Nature Publishing Group.
- [6] Mahsa Haghghattalab, Abdolmohammad Kajbafzadeh, Mostafa Baghani, Ziba Gharehnazifam, Bahareh Mohammadi Jobani, and Majid Baniassadi. Silk Fibroin Hy-

- drogel Reinforced With Magnetic Nanoparticles as an Intelligent Drug Delivery System for Sustained Drug Release. *Frontiers in Bioengineering and Biotechnology*, 10, 2022.
- [7] Shuya Ishii, Seiichi Saiki, Shinobu Onoda, Yuta Masuyama, Hiroshi Abe, and Takeshi Ohshima. Ensemble Negatively-Charged Nitrogen-Vacancy Centers in Type-Ib Diamond Created by High Fluence Electron Beam Irradiation. *Quantum Beam Science*, 6(1):2, March 2022. Number: 1 Publisher: Multidisciplinary Digital Publishing Institute.
- [8] Zeynep Karahaliloğlu, Eda Yalçın, Murat Demirbilek, and Emir Baki Denkbaş. Magnetic silk fibroin e-gel scaffolds for bone tissue engineering applications. *Journal of Bioactive and Compatible Polymers*, 32(6):596–614, November 2017. Publisher: SAGE Publications Ltd STM.
- [9] P. Kehayias, M. J. Turner, R. Trubko, J. M. Schloss, C. A. Hart, M. Wesson, D. R. Glenn, and R. L. Walsworth. Imaging crystal stress in diamond using ensembles of nitrogen-vacancy centers. *Physical Review B*, 100(17):174103, November 2019. Publisher: American Physical Society.
- [10] Edlyn V. Levine, Matthew J. Turner, Pauli Kehayias, Connor A. Hart, Nicholas Langelier, Raisa Trubko, David R. Glenn, Roger R. Fu, and Ronald L. Walsworth. Principles and techniques of the quantum diamond microscope. *Nanophotonics*, 8(11):1945–1973, November 2019. Publisher: De Gruyter.
- [11] Federico Ignacio Poggioli Pardo. Construction and Characterization of a Quantum Diamond Microscope. Technical report, Worcester Polytechnic Institute, 2021.
- [12] Kun-Yu Qian, Yonghong Song, Xu Yan, Liang Dong, Jingzhe Xue, Yunjun Xu, Bao Wang, Baoqiang Cao, Qingbing Hou, Wei Peng, Jinlong Hu, Kun Jiang, Sheng Chen, Huiqing Wang, and Yang Lu. Injectable ferrimagnetic silk fibroin hydrogel for magnetic hyperthermia ablation of deep tumor. *Biomaterials*, 259:120299, November 2020.
- [13] Romana Schirhagl, Kevin Chang, Michael Loretz, and Christian L. Degen. Nitrogen-Vacancy Centers in Diamond: Nanoscale Sensors for Physics and Biology. *Annual Review of Physical Chemistry*, 65(1):83–105, 2014. eprint: <https://doi.org/10.1146/annurev-physchem-040513-103659>.